

Identifying trend reversals in atmospheric ethane from a multi-site analysis

Abstract

Ethane is the most abundant non-methane hydrocarbon in Earth's atmosphere and acts as an indirect greenhouse gas, influencing the atmospheric lifetime of methane. Therefore, understanding the development of trends and identifying trend reversals in atmospheric ethane is crucial. Ethane abundance is measured at different ground-based stations worldwide using Fourier transform infrared remote sensing techniques. We compile a new dataset comprising 26 ethane time series from the Northern and Southern Hemispheres. We analyze their long-term trends using different econometric techniques capable of handling missing data and strong seasonal components present in the data. The resulting trend patterns are consistent across the different methods, with similar estimated trends at the various stations. In the Northern Hemisphere, the common trend across stations declined from the 1990s to 2005, gradually increased over the next decade, and then resumed a similar downward trajectory from 2015 onward. The estimated trends reveal a pronounced peak around 2014/2015, marking a reversal from an upward to a downward trend.

Keywords: atmospheric ethane, FTIR remote sensing, nonparametric trend analysis, Kalman filter

1 Introduction

Short-lived climate forcers are broadly divided into methane and non-methane volatile organic compounds (NMVOC) (Szopa et al., 2021). They affect the climate and are often also air pollutants. Ethane is the most abundant NMVOC in the atmosphere, sharing important emission sources with methane, a major greenhouse gas with high global warming potential (Franco et al., 2015). The main sources of ethane are anthropogenic (62% from leakage during production and transport of natural gas, 20% from biofuel combustion), while methane has both natural and anthropogenic sources (Xiao et al., 2008). Understanding trends in atmospheric ethane is crucial to better constrain the anthropogenic sources of methane, in particular from the oil and gas industry (Franco et al., 2016). The ethane abundance in the atmosphere is measured above many ground-based stations using Fourier transform infrared (FTIR) remote sensing techniques. Therefore, observational data is available for a wide spread of locations all over the world. However, trend patterns have only been analyzed in the literature for a subset of these locations.

Several papers have studied trends in atmospheric ethane. For example, Angelbratt et al. (2011) obtain ethane trends until 2006 from four different stations located in the Northern Hemisphere (NH). Zeng et al. (2012) obtain trend estimates until 2009 from the ethane burden above Lauder and Arrival heights. Franco et al. (2015) analyze the trending pattern observed over the Jungfraujoch measurement station. Franco et al. (2016) analyze ethane trends in North America with the support of model simulations. Lutsch et al. (2020) study 10 ethane time series from the NH until 2018. Friedrich et al. (2020a) investigate ethane trends from four different stations, one of them located in the Southern Hemisphere (SH); three of these end in 2014 and one in 2019. Recently, Maddanu and Proietti (2023) analyze ethane trends from 15 different stations until 2021, three of which are located in the SH. From this strand of the literature, we can see trend patterns emerging, which are common to most of the analyzed data sets. Most of the series obtained from stations in the NH share a similar trend pattern: a steady downward trend until around 2007/2008, followed by a significant upward trend. This trend reversal has been found in Franco et al. (2015), Lutsch et al. (2020), Friedrich et al. (2020a) and Maddanu and Proietti (2023). Subsequently, a slowdown of the upward trend around 2014/2015 has been found for the Jungfraujoch in Friedrich et al. (2020a). This is confirmed for some other NH stations in Maddanu and Proietti (2023), resulting in a second trend reversal that has received less attention in the literature up to this point. The SH stations, however, do not share a clear common trending pattern.

In this paper, we investigate the 2014/2015 trend reversal in a new dataset consisting of updated ethane measurements up to 2023 for a total of 26 stations (five from the SH). To understand the long-term developments of the ethane burden in the atmosphere, we carefully analyze the time trends obtained from each of the 26 stations. Our approach combines three distinct econometric techniques. Since FTIR ethane data display a large fraction of missing observations and a strong seasonal pattern, causing high correlation between data points over time, we adopt econometric methods that have been shown to account for these characteristics (Friedrich et al.,

2020b; Maddanu and Proietti, 2023). Specifically, we estimate smooth trends nonparametrically as in Friedrich et al. (2020a) to get a first impression of the trend at each station. This nonparametric approach allows us to extract a trend curve without making restrictive assumptions on the shape of the trend. We observe a pronounced peak around 2014/2015 in almost all of the estimated trends from the NH. To further validate this observed pattern, we employ a second method using parametric unobserved components models. The results align with the nonparametric analysis, reinforcing the robustness of our conclusions. The findings are also in line with the previous analysis of the ethane burden above the Jungfrauoch found in Friedrich et al. (2020a) and with results from Maddanu and Proietti (2023). To quantify the increase and subsequent decrease, we proceed by assuming (piecewise) linearity of the trend line. Based on this assumption, we test for a break in the linear trend at each station. If a break is present, we locate it and quantify the uncertainty around the break location. We report slopes (with bootstrap confidence intervals) before and after the break. We find evidence for a break in trend between 2013 and 2016 for almost all stations, with the exceptions of Paramaribo and St. Denis. In the NH, the estimated slope coefficient before the break is positive and ranges from 1.3 to 7.3% per year. After the break, it turns negative with magnitudes ranging from -0.4 to -2% per year. In the SH, there is no overall common pattern.

The remainder of the paper is organized as follows. In Section 2, we describe the data used for this study. Section 3 explains our general modeling strategy, while the following Sections 4–6 go into details about our three approaches and presents their results. Section 7 concludes.

2 The data

We study a new and extended dataset consisting of atmospheric ethane abundances recorded at 26 different measurement stations across the world. The data set consists of 21 series obtained from stations in the Northern Hemisphere (NH) and five from the Southern Hemisphere (SH). As shown in Figure 1, the stations are located across different latitudes and altitudes. More details on the exact location of the measurement stations are summarized in Table 1. The stations are sorted according to latitude in descending order. Eureka to Sodankyla are considered NH high-latitude stations, Harestua to Tsukuba are NH mid-latitude, and Izaña to Paramaribo NH subtropics and tropics stations. Both stations on La Réunion are categorized as SH subtropics and tropics, Wollongong and Lauder as SH mid-latitude, and Arrival Heights as SH high-latitude stations. We additionally observe that the measurement stations at Zugspitze, Jungfrauoch, Izaña, Mauna Loa, and Altzomoni are high-altitude stations, located higher than 2,500 meters above sea level.

The data cover a time span of more than 35 years, with the earliest observations going back to 1986 and the most recent ones obtained in 2023. We work with dry-air mole fractions (DAMF) in parts per billion (ppb) instead of with non-normalized ethane total columns expressed in the number of molecules per cm^2 . The DAMF corresponds to the ratio between the actual total column of the target gas, here ethane, and the dry-air pressure column. The way to compute DAMF is provided,

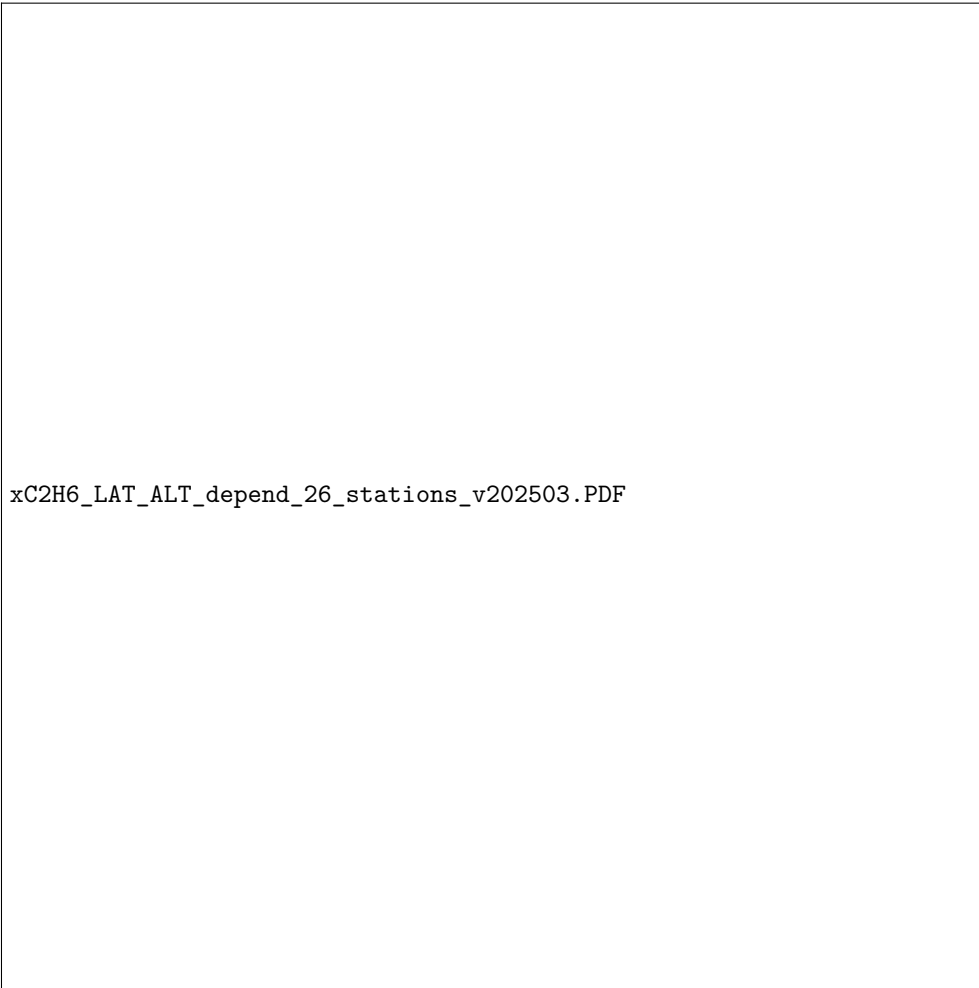


Fig. 1: Latitudinal variation of the ethane yearly mean dry air mole fraction, computed for (the year) 2019 (2018 for Wollongong). The additional effect of altitude is color-coded following the right panel scale. The full names and codes of the stations are listed in Table 1.

88 e.g., in [Pardo Cantos et al. \(2022\)](#), see Eq. (2) in Section 4.3.1). Whenever multiple
89 measurements are taken on one day, we consider daily averages.

90 The last column of Table 1 shows the percentage of missing data per station.
91 They are obtained as the number of days in the sample period of the respective sta-
92 tion in which no observations are available. With 45.52% of missing observations, the
93 series obtained at Xianghe, China, contains the highest ratio of observations, while
94 the Paramaribo series has the highest ratio of missing data with 96.89% (although

95 there are still 102 observations available). Several limiting factors can explain signif-
 96 icant fractions of missing data. The most important one is weather conditions since
 97 the ground-based FTIR technique requires a cloud-free sky to record spectra. Other
 98 unfavorable circumstances include instrumental failures and campaign-type observa-
 99 tions, which are generally limited in duration. These percentages clearly indicate that
 100 missing data is a severe and non-negligible problem in our analysis. In particular, com-
 101 mon imputation techniques such as linear interpolation are likely to be imprecise and
 102 may introduce strong biases into the outcomes. Therefore, we do not impute the data
 103 but use statistical methods that allow for missing values. A strong seasonal pattern
 104 further characterizes the data, as ethane degrades faster under warm weather condi-
 105 tions than in cold temperatures, and therefore, the measurements display local peaks
 106 every winter period. The seasonal pattern is clearly visible in Figure 2, which plots a
 107 subset of six series. From the NH, we select one mid-latitude station (Harestua), two
 108 mid-latitude stations – one of which is a high altitude (Jungfrauoch) and the other
 109 one a low altitude station (Karlsruhe) – as well as one station from the subtropics
 110 and tropics (Paramaribo). From the SH, we select one mid-latitude (Lauder) and one
 111 high-latitude station (Arrival Heights). Even though the displayed data have different
 112 sample lengths, the differences in data availability are visible. Lauder is the most com-
 113 plete among this subgroup with 64% of missing data, while Paramaribo is the most
 114 incomplete with almost 97% of missing data. As in Figure 2, we see that the overall
 115 burden is lower in the SH than in the NH and gets lower with decreasing latitude.
 116 Comparing the NH mid-latitude stations Jungfrauoch and Karlsruhe, we observe an
 117 expected lower average burden for the high-altitude station due to the altitude differ-
 118 ence. Commonalities in long-term behavior over time are, however, not evident from
 119 these plots due to the strong seasonality and missing observations. In the next section,
 120 we proceed with the extraction of long-term trends using statistical techniques.

121 3 A general set-up for long-term trend modeling

122 The trending behavior of ethane abundance may consist of long-run movements,
 123 seasonal fluctuations, and short-run variations. Hence, we consider the model

$$y_t = \mu_t + \psi_t + \varepsilon_t, \quad t = 1, \dots, T, \quad (1)$$

124 where y_t denotes the ethane abundance measured at a given station at day t , the
 125 variable μ_t represents the long-run trend component over years, which is the primary
 126 focus of our analysis, variable ψ_t captures seasonal effects within each year, and ε_t
 127 is a stochastic error term that accounts for short-run fluctuations in y_t . The technical
 128 statistical details of the different approaches are discussed below.

129 To draw solid conclusions about the trending behaviors of ethane abundance, we
 130 focus on the treatment of the trend component μ_t and remove the seasonal com-
 131 ponent ψ_t from the ethane time series y_t . In other words, we seasonally adjust
 132 the data a priori, which is a standard procedure in official statistics, for example,
 133 see <https://www.census.gov/data/software/x13as.html> (last accessed on August 22,
 134 2025). In this study, we analyze daily ethane measures and adopt the unobserved com-
 135 ponents time series model (UCTSM) for seasonal adjustment, see Appendix A.2. In

| Station | Code | Country | Location | Altitude | Range | Obs. | Missing | Reference |
|----------------------------|--------|---------------|-------------------|----------|-----------|-------|---------|--|
| <i>Northern Hemisphere</i> | | | | | | | | |
| Eureka | EUR | Canada | 80.05°N, 86.42°W | 610m | 2006-2020 | 828 | 83.40% | Batchelor et al. (2009) |
| Ny-Ålesund | NYA | Norway | 78.92°N, 11.93°E | 15m | 1993-2022 | 882 | 90.88% | |
| Thule | THU | Greenland | 76.52°N, 68.77°W | 225m | 1999-2022 | 1,537 | 81.71% | Hannigan et al. (2009) |
| Kiruna | KIR | Sweden | 67.80°N, 20.40°E | 420m | 1996-2022 | 1,962 | 79.85% | Blumenstock et al. (2009) |
| Sodankylä | SDK | Finland | 67.37°N, 26.63°E | 188m | 2012-2023 | 1,193 | 70.82% | Kivi and Heikkinen (2016) |
| Harestua | HAR | Norway | 60.2°N, 10.8°E | 596m | 1994-2021 | 1,224 | 87.62% | |
| St. Petersburg | SPB | Russia | 59.88°N, 29.83°E | 20m | 2009-2022 | 912 | 81.69% | Makarova et al. (2024) |
| Bremen | BRE | Germany | 53.10°N, 8.80°E | 27m | 2004-2022 | 548 | 91.85% | |
| Karlsruhe | KAR | Germany | 49.1°N, 8.42°E | 110m | 2010-2022 | 1,162 | 73.85% | Kiel et al. (2016) |
| Paris | PAR | France | 48.97°N, 2.37°E | 60m | 2011-2022 | 551 | 86.45% | |
| Zugspitze | ZUG | Germany | 47.25°N, 10.59°E | 2,964m | 1995-2023 | 2,564 | 74.82% | Hausmann et al. (2016) |
| Jungfraujoch | JUN | Switzerland | 46.55°N, 7.98°E | 3,580m | 1986-2022 | 3,174 | 76.39% | Franco et al. (2015); Zander et al. (2008) |
| Toronto | TOR | Canada | 43.66°N, 79.40°W | 174m | 2002-2022 | 2,377 | 67.78% | Yamanouchi et al. (2023) |
| Rikubetsu | RIK | Japan | 43.46°N, 143.77°E | 380m | 1995-2022 | 1,078 | 89.10% | |
| Boulder | BLD | United States | 39.99°N, 105.26°W | 1,634m | 2010-2021 | 973 | 79.07% | Ortega et al. (2019) |
| Xianghe | XIA | China | 39.75°N, 116.96°E | 46m | 2018-2021 | 706 | 45.52% | Zhou et al. (2023) |
| Tsukuba | TSU | Japan | 36.05°N, 140.12°E | 31m | 2001-2022 | 1,107 | 85.94% | |
| Izaña | IZA | Spain | 28.30°N, 16.50°W | 2,367m | 1999-2022 | 2,309 | 73.31% | García et al. (2021) |
| Mauna Loa | MLO | United States | 19.54°N, 155.58°W | 3,397m | 1995-2022 | 2,957 | 70.30% | Hannigan et al. (2009) |
| Altzomoni | ALT | Mexico | 19.12°N, 98.65°W | 3,985m | 2012-2023 | 1,176 | 69.44% | Baylon et al. (2017) |
| Paramaribo | PMB | Suriname | 5.74°N, 55.2°W | 23m | 2013-2022 | 102 | 96.89% | |
| <i>Southern Hemisphere</i> | | | | | | | | |
| La Réunion, St. Denis | REU_ST | France | 20.9°S, 55.5°E | 85m | 2004-2015 | 745 | 81.15% | Vigouroux et al. (2012) |
| La Réunion, Maïdo | REU_M | France | 21.1°S, 55.4°E | 2,155m | 2013-2019 | 1,095 | 56.08% | |
| Wollongong | WOL | Australia | 34.24°S, 150.52°E | 30m | 2007-2020 | 2,324 | 52.48% | Griffith et al. (2021) |
| Lauder | LAU | New Zealand | 45.04°S, 169.68°E | 370m | 1996-2022 | 3,504 | 63.56% | Zeng et al. (2012) |
| Arrival Heights | AHT | Antarctica | 77.83°S, 166.67°E | 184m | 1997-2022 | 1,170 | 87.61% | Zeng et al. (2012) |

Table 1: Information on the FTIR measurement stations. Obs. reports the number of days with observations, and the missing percentages are calculated as the number of days without observations divided by the total number of days in the sample range of each station. Stations are sorted according to decreasing latitude for the Northern Hemisphere and increasing latitude for the Southern Hemisphere.

136 [Harvey et al. \(1997\)](#) it is argued that the challenges of seasonal adjustment of weekly
 137 or daily data can be most effectively addressed within the UCTSM framework. The
 138 UCTSM requires both components to be specified as latent random processes. For
 139 example, the trend can be modeled as a random walk process, and the seasonal can
 140 be modeled as a stochastic Fourier process, see also the discussion in [Proietti \(2000\)](#).
 141 Once the model is formulated in state space form, the Kalman filter and related meth-
 142 ods are adopted to estimate the unknown parameters by maximum likelihood, and to
 143 extract the components μ_t and ψ_t using a smoothing method, see [Durbin and Koop-](#)
 144 [man \(2012\)](#). The seasonal adjustment is achieved by simply subtracting the estimate
 145 of ψ_t from the data.

146 The trend component μ_t in this study is treated by different statistical approaches,
 147 each with a distinct perspective. These methods may involve nonparametric or para-
 148 metric models, and the trend itself may be specified as either a deterministic or a
 149 random process. First, following [Friedrich et al. \(2020a\)](#), we assume that the trend
 150 μ_t is a deterministic yet fully unknown function of time, and we estimate it nonpara-
 151 metrically. Second, we can extract the trend from the UCTSM model that is used for
 152 the seasonal adjustment of the data. Third, to achieve a more structural interpreta-
 153 tion of the trend and understand its rate of change, we assume piecewise linearity and
 154 employ a parametric broken linear trend approach ([Perron and Zhu, 2005](#); [Friedrich](#)
 155 [et al., 2020a](#); [Beutner et al., 2023](#)). This method enables us to calculate the rates of
 156 increase and decrease both before and after the peak.

157 4 Nonparametric trend analysis

158 To gain an initial understanding of the long-term trend μ_t in Eq. (1), we first consider
 159 a nonparametric specification that imposes minimal assumptions on the form of the
 160 trend. Specifically, let

$$\mu_t = g(t/T), \quad t = 1, \dots, T, \quad (2)$$

161 where $g(\cdot)$ denotes a smooth (i.e., twice continuously differentiable) unknown func-
 162 tion defined on the interval $[0, 1]$. As is standard with this approach, we map all time
 163 points into the interval $[0, 1]$ by dividing by T . This results in a theoretically consis-
 164 tent approximation of g with increasingly dense observations in the interval $[0, 1]$ as
 165 T increases (see, e.g., [Robinson, 1989](#); [Cai, 2007](#)). This is mainly done for theoretic-
 166 al purposes and does not affect estimation in practice. Apart from the smoothness
 167 assumption, we do not need to restrict the functional form of the trend.

168 Our main goal is to estimate the function $g(\cdot)$ and quantify the uncertainty around
 169 this estimate, as it reflects the long-term trending behavior of ethane abundance. We
 170 apply the toolkit proposed in [Friedrich et al. \(2020a,b\)](#), employing a nonparamet-
 171 ric kernel estimator in combination with the autoregressive wild bootstrap (AWB)
 172 to construct confidence bands. The estimator requires a smoothing parameter known
 173 as the bandwidth $h > 0$. The choice typically depends on the context of the study,
 174 but data-driven procedures can assist with this selection. A common approach for
 175 time series data is the Modified Cross-Validation (MCV) approach proposed by [Chu](#)
 176 [and Marron \(1991\)](#), which has been adopted, for instance, in [Friedrich et al. \(2020a\)](#).
 177 Given the substantial amount of missing values in several records (see Table 1) and

178 the fact that some time series, such as Xianghe, are relatively short, selecting an opti-
179 mal bandwidth for each series individually is challenging or even infeasible. At the
180 same time, the smoothness of ethane abundance can reasonably be expected to be
181 comparable across stations within the same hemisphere, as emissions may be influ-
182 enced by common regional drivers. For this reason, we pool the time series within each
183 hemisphere and determine a single bandwidth per hemisphere, which allows shorter
184 records to “borrow” information from surrounding stations. This approach ensures a
185 common level of smoothness within hemispheres and thereby also facilitates compar-
186 isons between trends. Importantly, however, adopting a common h does not imply
187 that the trends themselves must evolve in the same direction or exhibit the same mag-
188 nitude. For this purpose, the MCV approach is adapted to account for multiple time
189 series, with the technical details provided in Appendix A. In our case, a bandwidth
190 of $h = 0.09$ is selected by the criterion for the NH and $h = 0.125$ for the SH.

191 Figure 3 displays the nonparametric trend estimates and 95%-level confidence
192 bands. The stations are sorted according to latitude in descending order. The DAMF
193 are plotted as grey circles, the black line is the estimated trend line, and the blue
194 lines are the confidence bands. Overall, the nonparametric trend estimates capture
195 the movement of ethane abundance at each station well.

196 To examine potential co-movements, we demean all estimated trend curves and
197 plot them together in Figure 4. Panel (a) includes all stations from the Northern Hemi-
198 sphere, and panel (b) all Southern Hemisphere. We find a pronounced peak around
199 2014/2015 for almost all series of the NH. For series that start early (e.g., Harestua,
200 Rikubetsu, Jungfrauoch, Zugspitze), we additionally see an overall downward trend
201 until around 2006-2009 – interrupted by a local peak around 1998 and 2002 (Yurganov
202 et al., 2004, 2005) – which then turns into an upward trend until the 2014/2015 peak.
203 It is important to emphasize the common tendency observed across the NH stations.
204 The common trend declined from the 1990s until around 2005. After that, it gradually
205 increased for about 10 years. This downward-upward trend reversal has been associ-
206 ated in the literature with an increasing shale gas exploitation in the United States
207 (Franco et al., 2015; Friedrich et al., 2020a; Maddanu and Proietti, 2023). However,
208 starting in 2015, the trend began to decline again at a pace similar to that seen in
209 the 1990s. This latest trend reversal has been tentatively attributed to the evolution
210 of the crude oil price which showed a severe reduction as of 2015 (Friedrich et al.,
211 2020a; Angot et al., 2021; Maddanu and Proietti, 2023). This affected the profitability
212 of fracking, possibly leading to a rapid reduction of related emissions, given the ver-
213 satility of the U.S. industry and economy.¹ It is interesting to note that Zhang et al.
214 (2024) found that the trend in the ethane emissions was decoupled from ethane pro-
215 duction, based on observations performed in the U.S. by the National Oceanic and
216 Atmospheric Administration (NOAA) Global Monitoring Laboratory. Indeed, they
217 report that US emissions would have risen by 0.25 ± 0.31 Tg over 2015-2020 while
218 reported ethane production increased by 78%. These authors provide several ways
219 to explain this decoupling, including the exploitation of new wells with lower ethane

¹In line with Franco et al. (2016) and Maddanu and Proietti (2023), we examine the correlation between the trend reversals identified by our nonparametric and parametric models and U.S. crude oil production as well as U.S. natural gas gross withdrawals in Appendix B.

220 content, and/or that leakage at the various phases of production (drilling, storage,
221 transport) may have diminished Zhang et al. (2024).

222 The 2014/2015 peak stands out as it appears across nearly all series in the NH.
223 Exceptions include Xianghe, which started only in 2018, and Mauna Loa, which had
224 multiple large gaps before the period of interest, complicating the accurate estimation
225 of the long-term trend during this time. For the other series, we will further analyze the
226 characteristics of the observed peak and the resulting trend reversal in the remaining
227 two sections.

228 We also observe that the SH exhibits less distinct common trends. However, we see
229 a downward-upward trend reversal for some locations, where early data is available.
230 The reversal is estimated to happen between 2010 and 2015, which is later than in the
231 NH. This could imply a delayed effect of the shale gas extraction in the SH compared
232 to the NH. Specifically, there is a common downward trend visible for Lauder and
233 Arrival Heights where observations are available before 2000. For Wollongong and La
234 Réunion St. Denis, the downward trend is also visible, even though the observations
235 start a bit later.

236 5 State-space modeling of trends

237 A parametric approach to trend estimation can be based on an unobserved compo-
238 nents time series model (UCTSM) that includes a trend component. We have discussed
239 the UCTSM in Section 2 for the purpose of seasonal adjustment, given that the
240 data from all stations are subject to year-on-year (trend) and within-year (seasonal)
241 changes. We therefore adopt a state-space approach based on the decomposition in
242 Eq. (1) in Section 3, with a long-term trend component μ_t and a seasonal effects
243 component ψ_t . We treat these components as unobserved dynamic processes and include
244 them jointly in the UCTSM; see Durbin and Koopman (2012). We have found that
245 the trend component μ_t in Eq. (1) can appropriately be specified as a smooth stochas-
246 tic trend function, represented by an integrated random walk process. Hence, the role
247 of μ_t is to account for the low-frequency year-on-year dynamics in the time series y_t .
248 Furthermore, the seasonal within-year component ψ_t has shown to be effective when
249 it is treated as a sum of S stochastically time-varying Fourier series corresponding
250 to the seasonal frequencies $2\pi j / 365.25$, with $j = 1, 2, 3$. More specific details of the
251 statical specifications of the trend and seasonal components, and the methodology to
252 estimate the model parameters and to extract the trend component, are reviewed in
253 Appendix A.2. A convenient feature of the state-space statistical treatment is that
254 missing observations, of which there are many in our data set, are treated as an
255 integrated part of the analysis.

256 5.1 Trend estimation results based on UCTSM

257 We apply the UCTSM framework to the ethane dry-air mole fractions. The results
258 are plotted in Figure 5. Each plot contains the original data, the corresponding trend
259 component estimate, and the 95%-level confidence interval. The start and end of
260 each time series plot can be different as the data availability for each station varies.
261 Although there are commonalities to be found in the trend estimates, they can also

262 be quite different among the different stations. Most trend estimates of the SH sta-
 263 tions have wider confidence intervals due to the shorter samples with larger amounts
 264 of missing values. Furthermore, the five estimated SH trends have lower values com-
 265 pared to most of the estimated NH trends. The estimated trends of the stations are
 266 jointly presented in Figure 4, the NH trends are presented in the left panel and the SH
 267 trends in the right panel. NH trends show some common patterns. Many NH trend
 268 estimates show increasing behavior between 2008 and 2015 or at least show upward
 269 trends in many of their sub-samples during this period. However, most stations show
 270 a downward trend after 2014/15. The trend of Thule stands out with a strong increas-
 271 ing pattern from 2000 onward. The trends from the SH stations do not provide a clear
 272 common pattern. The trend of Wollongong stands out with a strong increasing pat-
 273 tern from 2014 onward. To facilitate further comparisons, also between the trends of
 274 the nonparametric method and the UCTSM framework, we present in Figure B1, in
 275 Appendix B, the yearly means of the trend estimates from both approaches.

276 5.2 Trend breaks in 2014-2016 and percentage changes

277 To identify the most recent breaks in the trend estimates (in most cases, breaks in
 278 the years 2014-2016), we focus on the trend-slope estimates to detect the dates of the
 279 breaks. It can be observed that when the trend-slope component is negative, the trend
 280 is decreasing, and when the trend-slope is positive, the trend is increasing. Hence,
 281 when the trend-slope component switches its sign over time (its value is then close
 282 to zero when dealing with sufficiently smooth trends), the trend component shows a
 283 break from an increasing trend towards a decreasing trend (or vice versa). Therefore,
 284 the location of a break in the trend can be traced via the trend-slope estimate (at the
 285 position where it crosses the zero-line). When we locate the most recent zero-valued
 286 trend-slope estimate, we obtain the dates as presented in Table 2. We can interpret
 287 these dates as indicative of when the break has taken place. For many stations, no
 288 trend breaks can be detected because they are overall decreasing or increasing (no
 289 zero values found in the slope estimate). In cases where the trend is estimated as a
 290 fixed trend line, then no break is detected. When a break is identified, we measure
 291 the change in the trend level over the subsequent five years. Specifically, we report
 292 the percentage change in the trend value five years after the break date, given by

$$\%TrendChange = 100 \times \frac{TrendValue_{breakdate+5\ years} - TrendValue_{breakdate}}{TrendValue_{breakdate}}.$$

293 The results in Table 2 indicate that for 8 out of 21 stations in the NH, we have
 294 not detected a break in the trend in the last 7-8 years of the sample. Most of the 15
 295 break dates for the NH and SH stations occur either late in 2014 or in 2015, while
 296 the ones for Zugspitze and Boulder occur earlier in 2014, and for Wollongong, the
 297 (positive) break occurs in early 2016. All trend changes in the NH are negative, which
 298 implies that all trends decrease after the break dates. The only (slight) negative break
 299 detected within the five SH stations is for Maïdo, while the one for Wollongong is
 300 a positive break, implying an increasing trend after 17 February 2016. For the NH

| Station | Break Date | | | % Trend Change |
|----------------------------|------------|-------|-----|----------------|
| | Year | Month | Day | |
| <i>Northern Hemisphere</i> | | | | |
| Eureka | - | - | - | - |
| Ny-Ålesund | 2014 | 9 | 25 | -7.397 |
| Thule | - | - | - | - |
| Kiruna | 2015 | 7 | 23 | -11.95 |
| Sodankylä | 2014 | 9 | 22 | -5.609 |
| Harestua | - | - | - | - |
| St. Petersburg | 2015 | 2 | 23 | -7.886 |
| Bremen | 2014 | 6 | 29 | -10.22 |
| Karlsruhe | 2015 | 1 | 13 | -5.881 |
| Paris | 2014 | 11 | 18 | -0.289 |
| Zugspitze | 2014 | 4 | 30 | -3.308 |
| Jungfrauoch | 2015 | 6 | 26 | -15.01 |
| Toronto | 2014 | 10 | 22 | -8.284 |
| Rikubetsu | 2015 | 4 | 24 | -2.563 |
| Boulder | 2014 | 2 | 2 | -1.581 |
| Xianghe | - | - | - | - |
| Tsukuba | 2015 | 2 | 7 | -7.400 |
| Izaña | - | - | - | - |
| Mauna Loa | - | - | - | - |
| Altzomoni | - | - | - | - |
| Paramaribo | - | - | - | - |
| <i>Southern Hemisphere</i> | | | | |
| REU St. Denis | - | - | - | - |
| REU Maïdo | 2015 | 12 | 24 | -0.240 |
| Wollongong | 2016 | 2 | 17 | 2.081 |
| Lauder | - | - | - | - |
| Arrival Heights | - | - | - | - |

Table 2: Estimated ethane trend break points around 2015 and percentage trend change after five years, based on the UCTSM analysis.

301 stations, the largest trend changes of 7% and higher are detected for the stations Ny-
302 Ålesund, Kiruna, St. Petersburg, Bremen, Jungfrauoch, Toronto, and Tsukuba, while
303 trend changes closer to 3 – 5% are obtained for Sodankylä, Karlsruhe, and Zugspitze.

304 6 Direct approach to modeling trend breaks

305 The UCTSM framework discussed in Section 5 indicates that many stations exhibit
306 a trend break in 2015. In this section, we carry out a structural analysis using the
307 well-known broken linear trend model, originally proposed by Perron and Zhu (2005).
308 For related asymptotic results, see Harvey and Leybourne (2014) and Beutner et al.
309 (2023). Specifically, we assume that the trend follows a piecewise linear shape and
310 define μ_t as follows:

$$\mu_t = \alpha + \beta t + \delta D_{t,T_1}, \quad (3)$$

311 where $D_{t,T_1} = 0$ for $t \leq T_1$, and $t - T_1$ otherwise, with T_1 denoting the unknown
 312 break location. Eq. (3) describes a broken trend model with an unknown break point
 313 at T_1 . The intercept and slope parameters before the break are α and β , respectively.
 314 For $t > T_1$, the dummy variable D_{t,T_1} induces a change *solely* in the slope coefficient
 315 from β to $\beta + \delta$, while maintaining the intercept to ensure continuity at the break
 316 date. This prevents the modeled ethane concentration from exhibiting an abrupt and
 317 unrealistic jump at $t = T_1$. For the specification of the seasonal component ψ_t , we
 318 again adopt the Fourier series as in the previous sections (see Eq. (A10)).

319 The parameters of interest are (α, β, δ) , the parameters in the Fourier specification,
 320 and the unknown break date T_1 . We first test for the presence of a break using the test
 321 statistic F_T given in Friedrich et al. (2020a, Eq. (3.3)), which compares the sum of
 322 squared residuals of a model without break to the lowest sum of squared residuals of
 323 a model including one break. Critical values for the test are obtained with the AWB.
 324 Given a significance level of the test, the critical value of the test determines the cutoff
 325 point. If the test indicates evidence of a break, we estimate its location and obtain
 326 confidence intervals as in Friedrich et al. (2020a). We again use the autoregressive
 327 wild bootstrap for obtaining confidence intervals, as it has been theoretically shown
 328 to correctly mimic the missing data and variance patterns.

329 Since we want to focus on the 2014/2015 trend reversal pattern and the existing
 330 approach only allows for one trend break, we have to restrict the longer series to be
 331 able to capture our break point of interest. To this end, we disregard the data collected
 332 before 2004 in this analysis. The estimated break locations, slope coefficients, and
 333 confidence intervals obtained with the AWB are given in Table 3 for the NH and Table
 334 4 for the SH. If a break is detected by the test, the tables report the estimated slope
 335 coefficients $\hat{\beta}$ before the break and $\hat{\beta} + \hat{\delta}$ after the break. If no break is detected, the
 336 overall slope coefficient $\hat{\beta}$ is reported. The test results are reported in Table B1 in
 337 Appendix B.

338 The broken linear trend lines are plotted in Figure 6. The dry-air mole fraction
 339 data are plotted as grey circles. Furthermore, the seasonal fit is given by the black
 340 line, and the blue line shows the (broken) trend line. In cases where a break is present,
 341 the two dotted vertical lines show the confidence intervals around the break location
 342 corresponding to the results in Tables 3 and 4. In cases where no break is found by
 343 the test, only the trend line is displayed.

344 Several key observations can be made based on Tables 3 and 4 and Figure 6.
 345 First, we find evidence for a break in trend at a 10% significance level for almost
 346 all stations, with the exceptions of Eureka, Alzomoni, and Paramaribo in the NH
 347 and St. Denis in the SH. Second, if there is evidence for a break at an NH station,
 348 it is mostly located between 2013 and 2016, with confidence intervals spanning 2013
 349 until 2020 in the widest case (Boulder).² Two exceptions are Thule and Mauna Loa,
 350 with late breaks occurring in 2019 and 2021. Third, the estimated slope coefficient

² Note that for Boulder, the lower bound of the confidence interval for the break location coincides with the estimated break date. We note first that we employ a trim fraction of 0.1 at both the beginning and the end of the sample, as is standard in the literature for valid structural break tests (see also $\lambda = 0.1$ in the notation of Friedrich et al. (2020a)). After trimming, such a situation typically arises either when no structural break is present or when a break exists but its magnitude is too small to be accurately identified, in which case the confidence intervals may span the entire trimmed sample and the estimated break date (if any) may lie at the beginning or the end of the sample, depending on the data.

| Individual break dates and parameter estimates for the NH | | | | | |
|---|---------|--------------------|-------------------------------|----------------|---------------------------------|
| Station | Break | [CI] | Period | Slope (%) | [CI] (%) |
| Eureka | - | - | | 0.34 | [0.18, 0.51] |
| Ny-Ålesund | 2015.24 | [2013.73,2016.60] | <i>before</i> <i>after</i> | 0.83 -1.41 | [0.55, 1.10] [-1.81,-0.99] |
| Thule | 2019.64 | [2018.75,2020.24] | <i>before</i> <i>after</i> | 1.41 -1.60 | [1.31, 1.52] [-2.24,-1.03] |
| Kiruna | 2015.40 | [2014.23, 2016.35] | <i>before</i> <i>after</i> | 1.58 -1.25 | [1.37, 1.81] [-1.63,-0.88] |
| Sodankylä | 2014.85 | [2014.21,2015.43] | <i>before</i> <i>after</i> | 2.16 -1.78 | [1.24, 3.05] [-2.02,-1.55] |
| Harestua | 2015.19 | [2012.78,2017.12] | <i>before</i> <i>after</i> | 1.71 -0.90 | [1.28, 2.12] [-1.58,-0.24] |
| St.Petersburg | 2015.09 | [2014.57,2015.64] | <i>before</i> <i>after</i> | 2.95 -2.09 | [2.51, 3.41] [-2.47,-1.69] |
| Bremen | 2014.61 | [2013.75,2015.63] | <i>before</i> <i>after</i> | 2.43 -2.16 | [2.07, 2.80] [-2.58,-1.72] |
| Karlsruhe | 2013.90 | [2013.11,2015.20] | <i>before</i> <i>after</i> | 3.47 -0.53 | [2.50, 4.47] [-0.90,-0.17] |
| Paris | 2013.13 | [2012.39,2014.58] | <i>before</i> <i>after</i> | 8.80 -0.37 | [4.82, 11.5] [-0.87, 0.11] |
| Zugspitze | 2015.40 | [2014.44,2016.25] | <i>before</i> <i>after</i> | 1.67 -1.17 | [1.46, 1.86] [-1.49, 0.84] |
| Jungfraujoeh | 2015.65 | [2014.59,2016.75] | <i>before</i> <i>after</i> | 1.52 -1.19 | [1.31, 1.72] [-1.57,-0.81] |
| Toronto | 2014.86 | [2014.01,2015.67] | <i>before</i> <i>after</i> | 2.89 -1.86 | [2.55, 3.24] [-2.34,-1.33] |
| Rikubetsu | 2015.15 | [2014.02,2017.20] | <i>before</i> <i>after</i> | 1.48 -1.18 | [1.14, 1.81] [-1.81,-0.53] |
| Boulder | 2013.62 | [2013.62,2020.40] | <i>before</i> <i>after</i> | 4.46 -1.04 | [1.22, 7.48] [-1.61,-0.50] |
| Tsukuba | 2016.13 | [2015.02,2016.92] | <i>before</i> <i>after</i> | 1.54 -2.06 | [1.32, 1.78] [-2.60,-1.53] |
| Izaña | 2015.50 | [2014.24,2016.51] | <i>before</i> <i>after</i> | 1.37 -0.93 | [1.18, 1.57] [-1.23,-0.64] |
| Mauna Loa | 2021.37 | [2019.86,2021.86] | <i>before</i> <i>after</i> | 0.126 -2.61 | [0.04, 0.21] [-28.88,-1.74] |
| Altzomoni | - | - | | -0.16 | [-0.30,-0.02] |
| Paramaribo | - | - | | 0.24 | [-0.38, 0.92] |

Table 3: Point estimate and 95% confidence interval [CI] of the break date T_1 as well as the slope parameter β before and after the break in cases where we find evidence of a break in the time series, otherwise the overall slope is reported.

| Individual break dates and parameter estimates for the SH | | | | | |
|---|---------|--------------------|-------------------------------|---------------|---------------------------------|
| Station | Break | [CI] | Period | Slope (%) | [CI] (%) |
| La Réunion St.Denis | - | - | | -0.47 | [-0.64, -0.29] |
| La Réunion Maïdo | 2015.87 | [2015.58, 2016.27] | <i>before</i> <i>after</i> | 2.54 -1.80 | [2.04, 3.04] [-2.09, -1.50] |
| Wollongong | 2017.66 | [2017.10, 2019.72] | <i>before</i> <i>after</i> | -0.10 1.53 | [-0.18, -0.04] [1.16, 1.86] |
| Lauder | 2011.84 | [2009.63, 2013.86] | <i>before</i> <i>after</i> | -0.36 0.13 | [-0.45, -0.27] [0.07, 0.20] |
| Arrival Heights | 2014.61 | [2013.75, 2015.36] | <i>before</i> <i>after</i> | 2.43 -2.16 | [2.07, 2.80] [-2.58, -1.72] |

Table 4: Point estimate and 95% confidence interval [CI] of the break date T_1 as well as the slope parameter β before and after the break in cases where we find evidence of a break in the time series, otherwise the overall slope is reported.

351 before the break is positive and negative after the break in the NH. The corresponding
352 95% confidence intervals indicate that all pre-break slope estimates are significantly
353 different from zero. The post-break slopes of Paris and Zugspitze are the only ones
354 that are not significantly different from zero. The estimated slopes range from 0.8 to
355 8.8% per year before the break. After the break, they vary from -0.4 to -2.2% per
356 year. Fourth, in the SH, the common pattern is less clear. La Réunion Maïdo and
357 Arrival Heights share the NH pattern, with a break around 2015 and an upward-
358 downward trend pattern. La Réunion St. Denis shows a significant downward trend
359 and no evidence for a break. Note that the La Réunion stations are located in close
360 proximity but have little time overlap. Specifically, measurements at St. Denis end in
361 2015, while the time series at Maïdo begins in 2013. Wollongong and Lauder show a
362 downward-upward trend reversal between 2011 and 2017, similar to the early trend
363 reversal in the NH. This could again speak for a delayed effect of shale gas extraction
364 in the SH. Figure 4 is in line with the observed break results.

365 7 Conclusion

366 We analyzed a new dataset of atmospheric ethane abundance measured at 26 stations
367 around the globe. We assessed the trend patterns for each time series using three
368 distinct statistical approaches. These approaches have been selected because of their
369 ability to handle the large fraction of missing observations, autocorrelation as well as
370 heteroskedasticity in the data. The first two methods, namely the nonparametric and
371 UCTSM approaches, revealed that ethane trends in the Northern Hemisphere show
372 similar patterns. Specifically, both approaches identified a peak and subsequent trend
373 reversal from upward to downward around 2014/2015, with the NH trend declining

374 from the 1990s to 2005, rising for the next decade, and then declining again at a
 375 similar pace from 2015 onward.

376 To further investigate this trend reversal, we applied a broken linear trend model in
 377 two steps. First, we conducted a formal break test to determine whether a linear trend
 378 or a linear trend with one break provides a better fit to the data. Next, we estimated
 379 the (broken) trend model and reported the slope estimates, which indicate the annual
 380 percentage change. Our findings indicate that nearly all Northern Hemisphere stations
 381 show a breakpoint around 2014/2015. Prior to this breakpoint, the estimated slopes
 382 range from 0.8% to 8.8% per year, while after the breakpoint, they range from -0.4%
 383 to -2.2% per year. The confidence intervals indicate that most of these slopes are
 384 statistically significantly different from zero. More interestingly, for the majority of
 385 stations in the Northern Hemisphere, the intervals shift from positive to negative,
 386 suggesting a trend reversal from growth to decline. The three approaches applied in
 387 this paper should be seen as complementary rather than competing methods. Due to
 388 the characteristics of the data mentioned above, the extraction of trend reversals in the
 389 ethane burden can be a challenging task. By applying these methods in combination,
 390 they can provide stronger evidence of the presence of trend reversals in the data.

391 Overall, the consistency of our results across the different modeling approaches
 392 provides evidence that ethane levels in the Northern Hemisphere have been declining
 393 since 2015. In contrast, the Southern Hemisphere does not show a clear common
 394 trending pattern. While this most recent trend reversal in the Northern Hemisphere
 395 has been attributed to a decline in oil prices, it remains an interesting topic for future
 396 research. It would imply that we should later see the impact of the war in Ukraine,
 397 resulting in a renewed interest and related boom in fracking in the U.S. and elsewhere
 398 to cover the European need for non-Russian gas and oil. In addition, future research
 399 could explore the commonalities in these trending behaviors through multivariate
 400 statistical analysis and consider additional factors causing the observed trends, such
 401 as shale gas production. The methods applied in this paper may also be used in a
 402 forecasting exercise to predict future ethane abundances.

403 Appendix A Technical details

404 A.1 Nonparametric trend: a global smoothness parameter

405 To obtain a smoothness parameter that is optimal for multiple stations jointly, we first
 406 need to extend our nonparametric trend model to account for multiple time series:

$$y_{i,t} = \mu_{i,t} + \psi_{i,t} + \varepsilon_{i,t}, \quad i = 1, \dots, N, \quad t = 1, \dots, T, \quad (\text{A1})$$

407 where i is an index referring to station i with $i = 1, \dots, N$. Similarly, $\psi_{i,t}$ represents
 408 the seasonal effects of the i_{th} station at time t . To study the long-run comovement,
 409 we now specify $\mu_{i,t}$ as follows:

$$\mu_{i,t} = d_i + g(t/T), \quad i = 1, \dots, N, \quad t = 1, \dots, T, \quad (\text{A2})$$

410 where d_i is a deterministic term that captures the level of ethane for each individual
411 station. As in Section 4, the function $g(\cdot) : [0, 1] \rightarrow \mathbb{R}$ denotes a smooth, nonrandom
412 function that drives the variations of ethane globally. Hence, we drop the index i in
413 $g(\cdot)$. To formally account for missing data, we define a sequence of binary variables
414 $\{M_{i,t}\}$:

$$M_{i,t} = \begin{cases} 1, & \text{if } y_{i,t} \text{ is observed,} \\ 0, & \text{if } y_{i,t} \text{ is missing,} \end{cases} \quad i = 1, \dots, N, \quad t = 1 \dots, T, \quad (\text{A3})$$

415 where the missing data generating mechanism is assumed to satisfy the conditions
416 mentioned in Friedrich et al. (2020b).

417 Given the specification (A2), it is straightforward to obtain a consistent estimator
418 of $g(\cdot)$ by first partializing out the intercepts d_i and the seasonality component $\psi_{i,t}$
419 from $y_{i,t}$. As such, for each station i , we remove the seasonality of the ethane series
420 using the Fourier terms in (A10), then centralize/demean the data. We then obtain a
421 deseasonalized series $\{\tilde{y}_{i,t}, t = 1, \dots, T\}$ with zero average, i.e., $T^{-1} \sum_{t=1}^T M_{i,t} \tilde{y}_{i,t} = 0$,
422 $i = 1, \dots, N$.

423 We next consider the local linear estimation to estimate $g(\cdot)$. This nonparametric
424 estimation method has been previously adopted for trending panel data models, for
425 instance, see Li et al. (2011), Chen et al. (2012), Lin et al. (2023), and Friedrich et al.
426 (2025). More specifically, let $g^{(1)}(\cdot)$ be the first order derivative of $g(\cdot)$. Moreover, we
427 define $\tilde{\mathbf{y}}_i = (\tilde{y}_{i,1}, \dots, \tilde{y}_{i,T})'$ and $\mathbf{Z}(\tau) = (\mathbf{z}_1, \dots, \mathbf{z}_T)'$, where $\mathbf{z}_t(\tau) = (1, t/T - \tau)'$. For
428 every fixed $\tau \in [0, 1]$, then the local linear estimator of $g(\tau)$ is the first element in
429 $(\hat{g}(\tau), \hat{g}^{(1)}(\tau))'$, which is obtained by minimizing the following locally weighted sum
430 of squares:

$$\begin{aligned} \begin{pmatrix} \hat{g}(\tau) \\ \hat{g}^{(1)}(\tau) \end{pmatrix} &= \underset{(g(\tau), g^{(1)}(\tau))'}{\operatorname{argmin}} \sum_{i=1}^N \sum_{t=1}^T K\left(\frac{t/T - \tau}{h}\right) M_{i,t} \left[\tilde{y}_{i,t} - g(\tau) - g^{(1)}(\tau) (t/T - \tau) \right]^2 \\ &= \left[\sum_{i=1}^N \sum_{t=1}^T K\left(\frac{t/T - \tau}{h}\right) M_{i,t} \mathbf{z}_t(\tau) \mathbf{z}_t(\tau)' \right]^{-1} \left[\sum_{i=1}^N \sum_{t=1}^T K\left(\frac{t/T - \tau}{h}\right) M_{i,t} \mathbf{z}_t(\tau) \tilde{y}_{i,t} \right] \\ &= \left[\sum_{i=1}^N \mathbf{Z}(\tau)' \mathbf{W}_i(\tau, h) \mathbf{Z}(\tau) \right]^{-1} \sum_{i=1}^N \mathbf{Z}(\tau)' \mathbf{W}_i(\tau, h) \tilde{\mathbf{y}}_i, \end{aligned} \quad (\text{A4})$$

431 where $K(\cdot)$ is a kernel function, $h > 0$ is a use-specified bandwidth parameter, and

$$\mathbf{W}_i(\tau, h) = \operatorname{diag} \left\{ K\left(\frac{1/T - \tau}{T}\right) M_{i,1}, \dots, K\left(\frac{T/T - \tau}{T}\right) M_{i,T} \right\}, \quad i = 1, \dots, N, \quad (\text{A5})$$

432 are T -dimensional diagonal weighting matrices. The selection of $K(\cdot)$ usually does
433 not lead to a qualitative difference. We use the Epanechnikov kernel $K(x) = 3/4(1 -$
434 $x^2) \mathbb{1}_{\{|x| \leq 1\}}$ in our analysis. The bandwidth parameter h , which is *common* for all
435 i , controls the level of overall smoothness. As discussed in Section 4, a data-driven

436 method can assist the selection in practice. We consider the Modified Cross-Validation
 437 (MCV) loss criterion:

$$\text{MCV}(h) = (NT)^{-1} \sum_{i=1}^N \sum_{t=1}^T [\tilde{y}_{i,t} - \hat{g}_{l,h}(t/T)]^2, \quad (\text{A6})$$

438 where $\hat{g}_{l,h}(t/T)$ is the leave- $(2l+1)$ -out estimator obtained by omitting observations
 439 at $t = \lfloor \tau T \rfloor + i$, $-l \leq i \leq l$, $\tau \in [0, 1]$. We have that $(\hat{g}_{l,h}(\tau), \hat{g}_{l,h}^{(1)}(\tau))'$ equals

$$\left[\sum_{i=1}^N \sum_{t: |t-\tau T| > l} K\left(\frac{t/T - \tau}{h}\right) M_{i,t} \mathbf{z}_t \mathbf{z}_t' \right]^{-1} \left[\sum_{i=1}^N \sum_{t: |t-\tau T| > l} K\left(\frac{t/T - \tau}{h}\right) M_{i,t} \mathbf{z}_t \tilde{y}_{i,t} \right].$$

440 Conventionally, the optimal bandwidth \hat{h}_{opt} is the minimizer of the MCV criterion:

$$\hat{h}_{\text{opt}} = \underset{h \in \mathbb{H}}{\text{argmin}} \text{MCV}(h), \quad \mathbb{H} \subset \mathbb{R}. \quad (\text{A7})$$

441 Therefore, the method is fully data-driven whenever the value of l and the parameter
 442 space \mathbb{H} are specified.

443 We make the following remarks. Firstly, the leave- $(2l+1)$ -out estimator above
 444 only removes observations along the time dimension. Indeed, if N is sufficiently large,
 445 one may also implement the leave-one-unit-out cross-validation method by removing
 446 observations along the cross-sectional dimension as in [Chen et al. \(2012\)](#).

447 More importantly, the minimization step (A7) can be problematic, especially when
 448 constructing simultaneous confidence bands as discussed, for instance, in [Friedrich
 449 and Lin \(2024\)](#) and [Lin et al. \(2025\)](#). The issue mostly stems from the choice of \mathbb{H} ,
 450 more specifically here, the upper bound of \mathbb{H} . For illustration, we take $l = 0$ and
 451 $\mathbb{H} = \{0.05, 0.055, \dots, 0.245, 0.25\}$, yielding a grid of 41 points. For the global trend
 452 estimations, different values of l do not lead to a significant difference; the results are
 453 thus omitted. The MCV criteria using the data of the Northern and Southern Hemi-
 454 spheres are plotted in [Figure A1](#) separately. We observe that the loss function for the
 455 Northern Hemisphere monotonically decreases when $h \in \mathbb{H}$ is large enough. As such,
 456 the minimization rule (A7) often selects the upper bound of \mathbb{H} , making the results
 457 sensitive to the choice of \mathbb{H} . The figure also demonstrates that the MCV, or many
 458 other common data-driven methods, can have multiple local minima. For estimating
 459 $g(\cdot)$, we prefer a small bandwidth that can capture important, local movements in the
 460 trend curves while still producing a reasonably smooth estimate. Here we find that
 461 the second smallest local minimum for the Northern Hemisphere leads to satisfactory
 462 results, and the third one for the southern stations. Namely, we shall take the values
 463 of 0.09 and 0.125 for the Northern and Southern Hemispheres, respectively.

464 A.2 Unobserved components time series model

465 The unobserved components time series model (UCTSM) is considered for the seasonal
 466 adjustment of the ethane time series from all stations, see Section 2, and for the trend
 467 estimation in Section 5. The UCTSM is developed and explored in detail by Harvey
 468 (1989). It has a measurement equation that is the same as Eq. (1) and is given by

$$y_t = \mu_t + \psi_t + \varepsilon_t, \quad \varepsilon_t \stackrel{\text{i.i.d.}}{\sim} \mathcal{N}(0, \sigma_\varepsilon^2), \quad (\text{A8})$$

469 but we assume that the stochastic disturbance variable ε_t is independently and iden-
 470 tically distributed (i.i.d.), and has a Gaussian density with mean zero and variance
 471 $\sigma_\varepsilon^2 > 0$, that is $\mathcal{N}(0, \sigma_\varepsilon^2)$. The trend μ_t and seasonal ψ_t components are formulated as
 472 dynamic stochastic processes. The trend component μ_t is specified as an integrated
 473 random walk process given by

$$\mu_{t+1} = \mu_t + \beta_t, \quad \beta_{t+1} = \beta_t + \zeta_t, \quad \zeta_t \stackrel{\text{i.i.d.}}{\sim} \mathcal{N}(0, \sigma_\zeta^2), \quad (\text{A9})$$

474 where β_t is the growth, gradient or slope of μ_t and ζ_t is the innovation or disturbance
 475 driving the time-varying trend component. The disturbances ε_t in Eq. (A8) and ζ_t
 476 in Eq. (A9) are assumed to be mutually and serially independent of each other. The
 477 role of μ_t is to account for the low-frequency year-on-year dynamics in the time series
 478 y_t . The seasonal within-year component ψ_t is modeled as a sum of three dynamic
 479 stochastic processes specified as time-varying Fourier series with different seasonal
 480 frequencies. In particular, we have

$$\psi_t = \sum_{s=1}^S \psi_t^{(s)}, \quad (\text{A10})$$

481 where each individual Fourier process $\psi_t^{(s)}$ is specified as

$$\begin{pmatrix} \psi_{t+1}^{(s)} \\ \psi_{t+1}^{(s)*} \end{pmatrix} = \begin{bmatrix} \cos \lambda_s & \sin \lambda_s \\ -\sin \lambda_s & \cos \lambda_s \end{bmatrix} \begin{pmatrix} \psi_t^{(s)} \\ \psi_t^{(s)*} \end{pmatrix} + \begin{pmatrix} \omega_t^{(s)} \\ \omega_t^{(s)*} \end{pmatrix}, \quad (\text{A11})$$

482 and

$$\lambda_s = \frac{2\pi s}{365.25}, \quad \omega_t^{(s)}, \omega_t^{(s)*} \stackrel{\text{i.i.d.}}{\sim} \mathcal{N}(0, \sigma_\omega^2), \quad s = 1, \dots, S.$$

483 The disturbances ε_t in Eq. (A8), ζ_t in Eq. (A9) and $\omega_t^{(s)}$ and $\omega_t^{(s)*}$ in Eq. (A11) are
 484 assumed to be mutually and serially independent of each other, at all time points,
 485 and for all $s = 1, \dots, S$. All seasonal disturbances are assumed to share the same
 486 variance σ_ω^2 to keep the number of unknown parameters to a minimum. The dynamic
 487 specification for $\psi_t^{(s)}$ in Eq. (A11) relies fully on the auxiliary variable $\psi_t^{(s)*}$ that plays
 488 a similar role to β_t in Eq. (A9). The choice of the number of time-varying Fourier
 489 terms, S , can be based on formal statistical procedures such as the likelihood ratio
 490 (LR) test or the well-known Akaike information criterion (AIC). The specification
 491 of the UCTSM is completed with appropriate initial conditions for the unobserved

492 components and their auxiliary variables β_t and $\psi_t^{(s)*}$. We refer to the discussion in
 493 [Durbin and Koopman \(2012, Ch. 5\)](#) on initialization issues for the recursions in Eqs.
 494 (A9) and (A11). Alternative specifications for the seasonal component in a UCTSM
 495 are discussed by [Proietti \(2000\)](#).

496 The UCTSM can be formulated as a linear Gaussian state space model consisting
 497 of an observation equation for y_t and an update equation for the state vector α_t
 498 comprising all unobserved components together with their auxiliary variables. For our
 499 model with $S = 3$, we have

$$\alpha_t = \left(\mu_t, \beta_t, \psi_t^{(1)}, \psi_t^{(1)*}, \psi_t^{(2)}, \psi_t^{(2)*}, \psi_t^{(3)}, \psi_t^{(3)*} \right)'$$

500 The state space model has the general observation equation $y_t = \mathbf{Z}\alpha_t + \varepsilon_t$, with the
 501 selection matrix \mathbf{Z} which for the UCTSM (A8) is given by $\mathbf{Z} = (1, 0, 1, 0, 1, 0, 1, 0)$,
 502 and the state updating equation $\alpha_{t+1} = \mathbf{T}\alpha_t + \boldsymbol{\eta}_t$, with, following from Eqs. (A9)
 503 and (A11), the transition matrix \mathbf{T} as given by

$$\mathbf{T} = \begin{bmatrix} 1 & 1 & 0 & 0 & 0 & 0 & 0 & 0 \\ 0 & 1 & 0 & 0 & 0 & 0 & 0 & 0 \\ 0 & 0 & \cos \lambda_1 & \sin \lambda_1 & 0 & 0 & 0 & 0 \\ 0 & 0 & -\sin \lambda_1 & \cos \lambda_1 & 0 & 0 & 0 & 0 \\ 0 & 0 & 0 & 0 & \cos \lambda_2 & \sin \lambda_2 & 0 & 0 \\ 0 & 0 & 0 & 0 & -\sin \lambda_2 & \cos \lambda_2 & 0 & 0 \\ 0 & 0 & 0 & 0 & 0 & 0 & \cos \lambda_3 & \sin \lambda_3 \\ 0 & 0 & 0 & 0 & 0 & 0 & -\sin \lambda_3 & \cos \lambda_3 \end{bmatrix}$$

and with the state disturbance vector $\boldsymbol{\eta}_t = (0, \zeta_t, \omega_t^{(1)}, \omega_t^{(1)*}, \omega_t^{(2)}, \omega_t^{(2)*}, \omega_t^{(3)}, \omega_t^{(3)*})'$.
 The variance matrix of the state disturbance vector is given by

$$\boldsymbol{\Sigma}_\eta = \begin{bmatrix} 0 & 0 & 0 \\ 0 & \sigma_\zeta^2 & 0 \\ 0 & 0 & \sigma_\omega^2 \mathbf{I}_6 \end{bmatrix},$$

504 where \mathbf{I}_p is the $p \times p$ identity matrix. These system matrices \mathbf{Z} , \mathbf{T} , $\boldsymbol{\Sigma}_\eta$ and σ_ε^2
 505 determine the dynamic and statistical properties for y_t as implied by the UCTSM.
 506 Furthermore, the system matrices can partly depend on a set of unknown parameters,
 507 which for this UCTSM are only in σ_ε^2 and $\boldsymbol{\Sigma}_\eta$. We collect the unknown variances in
 508 the parameter vector $\boldsymbol{\phi} = (\sigma_\varepsilon^2, \sigma_\zeta^2, \sigma_\omega^2)'$.

509 Once the model is represented in state space form, the Kalman filter and related
 510 state space methods can be applied. The initialization of the Kalman filter recursions
 511 is based on the assumption of having a diffuse prior for α_1 . A particularly conve-
 512 nient feature of state space methods is that they can handle missing observations
 513 in a statistically correct manner. We estimate the unknown parameters in $\boldsymbol{\phi}$ by the
 514 method of maximum likelihood; the numerical maximization of the likelihood func-
 515 tion with respect to the parameter vector $\boldsymbol{\phi}$ requires the Kalman filter to compute

516 the log likelihood function repeatedly during the maximization process. Once the esti-
517 mate of ϕ is obtained, we can compute the standardized prediction errors from the
518 Kalman filter and use these for diagnostic checking and model evaluations. For both
519 seasonal adjustment and trend extraction, We require the smoothed estimates of the
520 unobserved trend μ_t and the periodic within-year component ψ_t , these are estimates
521 based on all observations. We can obtain them from a Kalman filter (forward step)
522 and a related smoothing method (backward step). More specific details of the state
523 space formulation and the state space methods are discussed in [Durbin and Koopman](#)
524 [\(2012\)](#).

525 Appendix B Additional outputs

526 In this section, we present additional results. Figure [B1](#) presents the yearly mean trend
527 estimates from both the nonparametric and state-space approaches. To highlight the
528 trend reversal around 2014/2015, we focus on the period 2010–2020. The outcome of
529 the break tests that aided the results in Section [6](#) are given in Table [B1](#). It shows
530 the sample period, the number of observations T together with the p -value, the test
531 statistic (F_T), and the AWB critical value associated with the break test at a signifi-
532 cance level of 5%. Low (high) values of F_T indicate little (substantial) evidence in
533 favor of the model with a structural break. We can see that the test detects a break in
534 all time series with the exception of Eureka, Altzomoni, Paramaribo, and St. Denis.

535 Additionally, we investigate the residuals obtained from our models using a Ljung-
536 Box test. In Table [B2](#), the results of Ljung-Box tests for residual autocorrelation,
537 including up to 20 lags, are given. The columns present the test statistics applied to
538 residuals from the nonparametric trend model of Section [4](#), the UCTSM model of
539 Section [5](#), and the (broken) linear trend model of Section [6](#). Given the high values of
540 the test statistics, the results indicate that there is remaining autocorrelation present
541 in the residuals of most models. This further underlines the need to apply robust
542 inference methods, such as the autoregressive wild bootstrap, which is employed in
543 Sections [4](#) and [6](#).

544 Finally, we perform a bivariate correlation analysis between the (monthly aver-
545 aged) estimated trends from the UCTSM model and a set of potential explanatory
546 variables. Those are the monthly U.S. production of crude oil, U.S. gross withdrawals
547 of natural gas, and U.S. gross withdrawals of shale gas, obtained from the U.S. Energy
548 Information Administration (<https://www.eia.gov>). The results are presented in Table
549 [B3](#). The columns give the pairwise Pearson correlation coefficient for crude oil pro-
550 duction, natural gas, and shale gas withdrawals, respectively. In addition, ***, **,
551 and * denote that the coefficient is statistically different from zero at the 0.01, 0.05,
552 and 0.1 level, respectively. Note that the statistical significance should be interpreted
553 with caution, given the strong persistence in the series. Although this analysis should
554 therefore be seen as a descriptive rather than a formal statistical analysis, it can shed
555 some light on the relation between ethane trends, and oil and gas production. Most
556 estimated trends from the Northern Hemisphere show a positive and significant cor-
557 relation with the explanatory variables. Exceptions are Ny-Ålesund, St. Petersburg,
558 Jungfrauoch, Boulder, Xianghe, and Altzomoni, where some of the coefficients are

559 negative and significant. In the Southern Hemisphere, the estimated trends mostly
560 exhibit a significantly negative correlation with the oil, gas, and shale gas variables
561 (with the exception of Wollongong). The average correlations between all three vari-
562 ables and the estimated trends are positive in the Northern Hemisphere and negative
563 in the Southern Hemisphere. These results are mostly in line with [Maddanu and Proietti \(2023\)](#)
564 who perform a regression analysis of the estimated trends on U.S. crude
565 oil production and U.S. natural gas gross withdrawals.

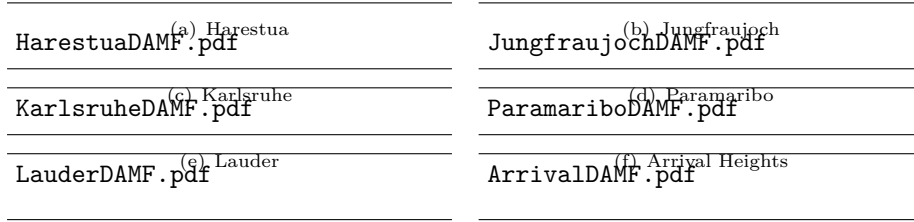


Fig. 2: Temporal development of ethane DAMF data in ppb obtained from different measurement stations. Note that the length of the sample differs for each station, which can make the seasonality and data availability appear more or less dense.

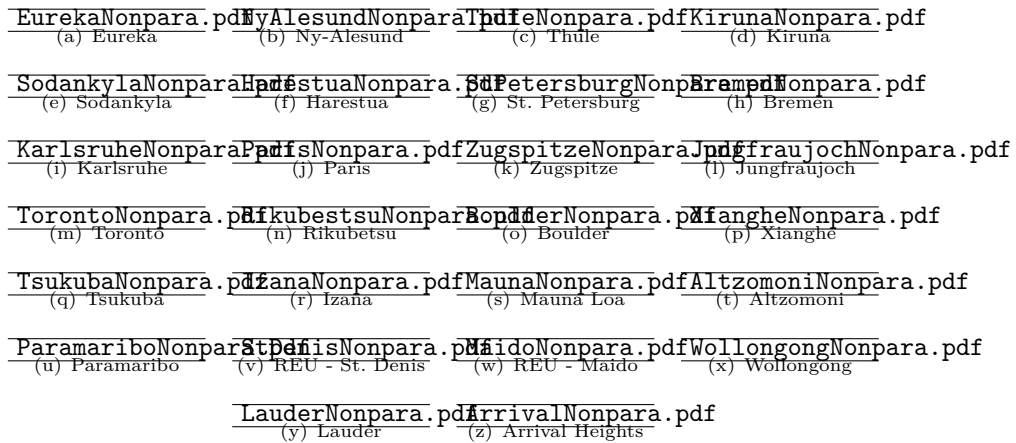


Fig. 3: Nonparametric trend results for all stations. Dry-air mole fractions (in ppb) are represented by the grey circles, the trend estimate by the black line (with bandwidths $h = 0.09$ for NH and $h = 0.125$ for SH), and the blue lines indicate the 95% confidence bands.



Fig. 4: Demeaned trend lines for all stations to compare comovements. Panels (a) and (b) show the nonparametrically estimated trends, while panels (c) and (d) show the estimated UCTSM trends for the Northern (left panels) and Southern Hemisphere (right panels). Note that in the left panels, the brown lines represent the estimated trends for Jungfraujoch, which is the longest time series shown.

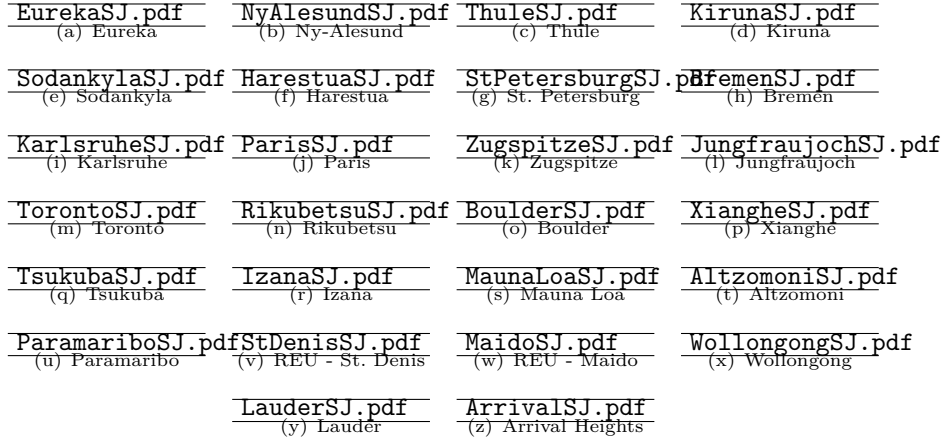


Fig. 5: Estimated UCTSM trends results for all stations. Dry-air mole fractions (in ppb) are given as grey circles, the trend estimate by the black line and the blue lines indicate the 95% confidence intervals.



Fig. 6: Results of the linear trend analysis as in Friedrich et al. (2020a). Dry-air mole fractions in ppb are given by the grey circles, the (broken) linear trend by the blue line, and the seasonal fit of the UCTSM by the black line. The dotted vertical lines (if present) are the confidence intervals around the break location.

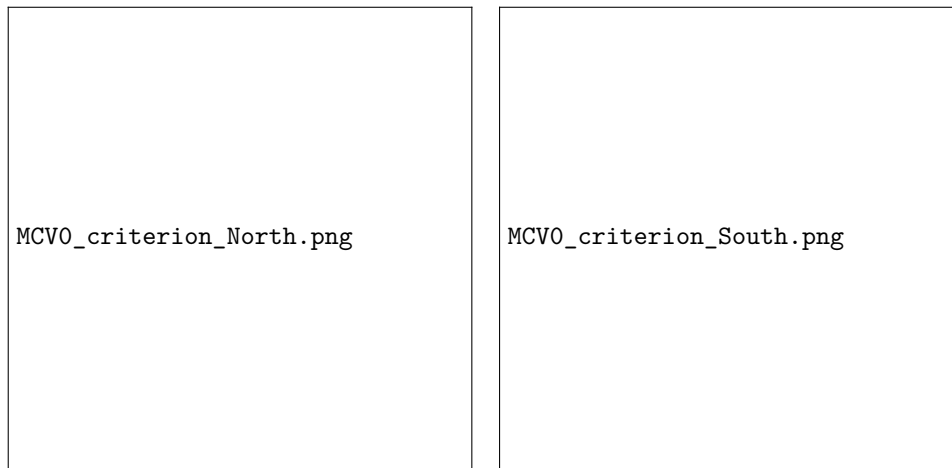
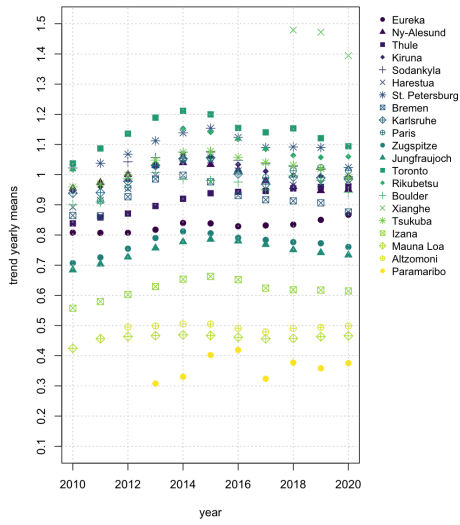
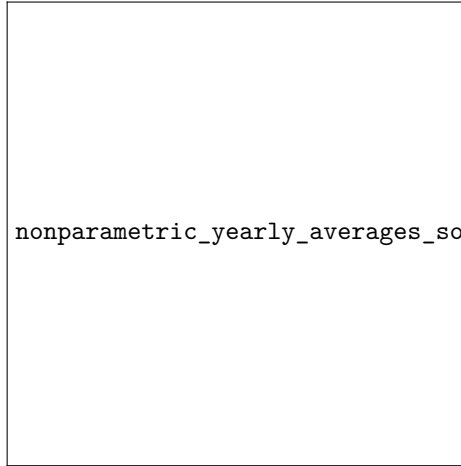


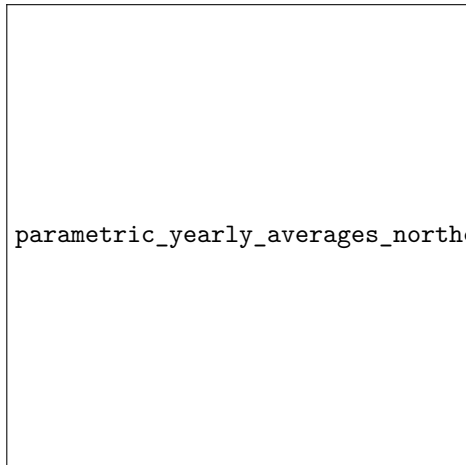
Fig. A1: Modified Cross-Validation (MCV) criterion over an equidistant grid of 41 points in $[0.05, 0.25]$ with a mesh of 0.005, based on the leave- $(2l + 1)$ -out estimator with $l = 0$. For the stations in the Northern Hemisphere (left), the two local minima are located at 0.065, and 0.09. For the stations in the Southern Hemisphere (right), the three local minima are located at 0.06, 0.095 and 0.125



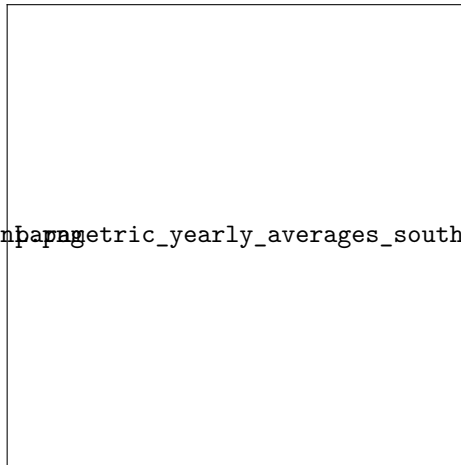
(a) Northern Hemisphere, Nonparametric



(b) Southern Hemisphere, Nonparametric



(c) Northern Hemisphere, UCTSM



(d) Southern Hemisphere, UCTSM

Fig. B1: Yearly mean trend estimates (2010–2020) obtained from the nonparametric method in Section 4 and from the UCTSM approach in Section 5. Stations are sorted according to decreasing latitude for the Northern Hemisphere and increasing latitude for the Southern Hemisphere.

| Station | Period | T | p -value | S_T | critical value |
|----------------------------|-----------|-------|------------|-------|----------------|
| <i>Northern Hemisphere</i> | | | | | |
| Eureka | 2006-2020 | 828 | 0.229 | 0.035 | 0.072 |
| Ny-Ålesund | 1993-2022 | 882 | 0.000 | 0.654 | 0.124 |
| Thule | 1999-2021 | 1,464 | 0.000 | 0.518 | 0.096 |
| Kiruna | 1996-2022 | 1,924 | 0.000 | 1.779 | 0.191 |
| Harestua | 1994-2021 | 1,224 | 0.000 | 0.670 | 0.178 |
| St. Petersburg | 2009-2022 | 906 | 0.000 | 2.150 | 0.167 |
| Bremen | 2004-2022 | 544 | 0.000 | 2.086 | 0.154 |
| Karlsruhe | 2010-2022 | 1,162 | 0.000 | 0.843 | 0.115 |
| Paris | 2011-2022 | 551 | 0.002 | 0.498 | 0.185 |
| Zugspitze | 1995-2020 | 2,237 | 0.000 | 2.834 | 0.215 |
| Jungfrauoch | 1986-2022 | 3,171 | 0.000 | 5.662 | 0.296 |
| Toronto | 2002-2022 | 2,377 | 0.000 | 9.039 | 0.865 |
| Rikubetsu | 1995-2022 | 1,078 | 0.000 | 0.451 | 0.102 |
| Boulder | 2010-2021 | 788 | 0.030 | 0.396 | 0.339 |
| Xianghe | 2018-2021 | 706 | | | |
| Tsukuba | 2001-2022 | 1,089 | 0.000 | 1.539 | 0.121 |
| Izaña | 1999-2021 | 2,244 | 0.000 | 1.792 | 0.170 |
| Mauna Loa | 1995-2021 | 2,746 | 0.000 | 0.135 | 0.041 |
| Altzomoni | 2012-2022 | 1,140 | 0.683 | 0.007 | 0.038 |
| Paramaribo | 2013-2022 | 102 | 0.126 | 0.026 | 0.037 |
| <i>Southern Hemisphere</i> | | | | | |
| La Réunion, St. Denis | 2004-2015 | 745 | 0.383 | 0.042 | 0.121 |
| La Réunion, Maïdo | 2013-2019 | 1,095 | 0.000 | 0.448 | 0.037 |
| Wollongong | 2007-2020 | 2,324 | 0.000 | 0.267 | 0.036 |
| Lauder | 1996-2022 | 3,426 | 0.000 | 0.089 | 0.014 |
| Arrival Heights | 1997-2022 | 1,130 | 0.000 | 0.017 | 0.002 |

Table B1: Results from the bootstrapped break test of [Friedrich et al. \(2020a\)](#) (with $\lambda = 0.1$), sorted according to latitude.

| Station | Nonpara. trend | UCTSM | Lin. trend |
|----------------------------|----------------|--------|------------|
| <i>Northern Hemisphere</i> | | | |
| Eureka | 112.00 | 121.10 | 114.75 |
| Ny-Ålesund | 383.04 | 62.42 | 322.82 |
| Thule | 172.26 | 200.67 | 193.93 |
| Kiruna | 513.53 | 153.61 | 443.16 |
| Harestua | 113.26 | 73.40 | 324.32 |
| St. Petersburg | 118.98 | 91.18 | 106.99 |
| Bremen | 35.34 | 55.54 | 52.25 |
| Karlsruhe | 94.95 | 72.46 | 100.41 |
| Paris | 54.32 | 47.27 | 48.42 |
| Zugspitze | 161.00 | 100.48 | 194.97 |
| Jungfrauoch | 349.95 | 168.00 | 225.86 |
| Toronto | 90.39 | 67.14 | 123.99 |
| Rikubetsu | 266.87 | 29.22 | 45.12 |
| Boulder | 33.17 | 35.78 | 29.98 |
| Xianghe | 33.73 | 22.51 | – |
| Tsukuba | 23.63 | 23.62 | 50.31 |
| Izaña | 189.69 | 214.45 | 198.15 |
| Mauna Loa | 813.53 | 863.88 | 671.88 |
| Altzomoni | 242.34 | 226.46 | 217.87 |
| Paramaribo | 18.45 | 37.62 | 35.31 |
| <i>Southern Hemisphere</i> | | | |
| La Réunion, St. Denis | 590.20 | 248.19 | 217.03 |
| La Réunion, Maïdo | 232.58 | 229.07 | 528.30 |
| Wollongong | 2398.09 | 381.49 | 425.80 |
| Lauder | 1726.82 | 219.80 | 1142.64 |
| Arrival Heights | 1254.57 | 42.81 | 920.62 |

Table B2: Test statistics from Ljung-Box tests for residual autocorrelation on the residuals of each model. The test is performed with 20 lags.

| Station | Crude oil | Natural gas | Shale gas |
|----------------------------|---------------|---------------|---------------|
| <i>Northern Hemisphere</i> | | | |
| Eureka | 0.976*** | 0.933*** | 0.957*** |
| Ny-Ålesund | -0.176*** | -0.348*** | -0.07 |
| Thule | 0.856*** | 0.874*** | 0.897*** |
| Kiruna | 0.506*** | 0.421*** | 0.324*** |
| Harestua | 0.606*** | 0.483*** | 0.507*** |
| St. Petersburg | 0.101 | -0.153** | -0.093 |
| Bremen | 0.292*** | 0.199*** | -0.088 |
| Karlsruhe | 0.355*** | 0.216*** | 0.217*** |
| Paris | 0.534*** | 0.296*** | 0.337*** |
| Zugspitze | 0.551*** | 0.423*** | 0.362*** |
| Jungfrauoch | 0.423*** | -0.139*** | 0.360*** |
| Toronto | 0.591*** | 0.501*** | 0.398*** |
| Rikubetsu | 0.389*** | 0.273*** | 0.398*** |
| Boulder | -0.023 | -0.291*** | -0.240*** |
| Xianghe | 0.243 | -0.490*** | -0.805*** |
| Tsukuba | 0.496*** | 0.346*** | 0.174** |
| Izaña | 0.704*** | 0.622*** | 0.469*** |
| Mauna Loa | 0.162*** | -0.027 | 0.559*** |
| Altzomoni | -0.588*** | -0.659*** | -0.745*** |
| Paramaribo | 0.755*** | 0.881*** | 0.931*** |
| Average North | 0.360 | 0.218 | 0.223 |
| <i>Southern Hemisphere</i> | | | |
| La Réunion, St. Denis | -0.823*** | -0.933*** | -0.977*** |
| La Réunion, Maïdo | -0.243** | -0.249** | -0.261** |
| Wollongong | 0.455*** | 0.557*** | 0.492*** |
| Lauder | -0.215*** | -0.353*** | 0.111 |
| Arrival Heights | -0.275*** | -0.390*** | 0.040 |
| Average South | -0.220 | -0.274 | -0.119 |

Table B3: Correlation analysis between the monthly averaged estimated UCTSM trends per station and time series of U.S. crude oil production, U.S. natural gas gross withdrawals and U.S. shale gas withdrawals. The values indicate the pairwise Pearson correlation coefficient, ***, ** and * denote that the coefficient is statistically different from zero at the 0.01, 0.05 and 0.1 level, respectively.

566 **References**

- 567 Angelbratt, J., Mellqvist, J., Simpson, D., Jonson, J. E., Blumenstock, T., Borsdorff,
568 T., Duchatelet, P., Forster, F., Hase, F., Mahieu, E., De Mazière, M., Notholt,
569 J., Petersen, A. K., Raffalski, U., Servais, C., Sussmann, R., Warneke, T., and
570 Vigouroux, C. (2011). Carbon monoxide (co) and ethane (c₂h₆) trends from
571 ground-based solar FTIR measurements at six European stations, comparison and
572 sensitivity analysis with the EMEP model. *Atmospheric Chemistry and Physics*,
573 11(17):9253–9269.
- 574 Angot, H., Davel, C., Wiedinmyer, C., Pétron, G., Chopra, J., Hueber, J., Blanchard,
575 B., Bourgeois, I., Vimont, I., Montzka, S. A., Miller, B. R., Elkins, J. W., and
576 Helmig, D. (2021). Temporary pause in the growth of atmospheric ethane and
577 propane in 2015–2018. *Atmospheric Chemistry and Physics*, 21(19):15153–15170.
- 578 Batchelor, R. L., Strong, K., Lindenmaier, R., Mittermeier, R. L., Fast, H., Drum-
579 mond, J. R., and Fogal, P. F. (2009). A new bruker IFS 125hr FTIR spectrometer
580 for the polar environment atmospheric research laboratory at Eureka, Nunavut,
581 Canada: Measurements and comparison with the existing Bomem DA8 spectrome-
582 ter. *Journal of Atmospheric and Oceanic Technology*, 26(7):1328 – 1340.
- 583 Baylon, J. L., Stremme, W., Grutter, M., Hase, F., and Blumenstock, T. (2017).
584 Background CO₂ levels and error analysis from ground-based solar absorption
585 IR measurements in central Mexico. *Atmospheric Measurement Techniques*,
586 10(7):2425–2434.
- 587 Beutner, E., Lin, Y., and Smeekes, S. (2023). GLS estimation and confidence sets for
588 the date of a single break in models with trends. *Econometric Reviews*, 42(2):195–
589 219.
- 590 Blumenstock, T., Hase, F., Kramer, I., Mikuteit, S., Fischer, H., Goutail, F., and Raf-
591 falski, U. (2009). Winter to winter variability of chlorine activation and ozone loss
592 as observed by ground-based FTIR measurements at Kiruna since winter 1993/94.
593 *International Journal of Remote Sensing*, 30(15-16):4055–4064.
- 594 Cai, Z. (2007). Trending time-varying coefficient time series models with serially
595 correlated errors. *Journal of Econometrics*, 136:163–188.
- 596 Chen, J., Gao, J., and Li, D. (2012). Semiparametric trending panel data models with
597 cross-sectional dependence. *Journal of Econometrics*, 171(1):71–85.
- 598 Chu, C.-K. and Marron, J. S. (1991). Comparison of two bandwidths selectors with
599 dependent errors. *Annals of Statistics* 19(4), pages 1906–1918.
- 600 Durbin, J. and Koopman, S. J. (2012). *Time Series Analysis by State Space Methods*.
601 Oxford: Oxford University Press, 2nd edition.
- 602 Franco, B., Bader, W., Toon, G. C., Bray, C., Perrin, A., Fischer, E. V., Sudo, K.,
603 Boone, C. D., Bovya, B., Lejeune, B., Servais, C., and Mahieu, E. (2015). Retrieval
604 of ethane from ground-based FTIR solar spectra using improved spectroscopy:
605 Recent burden increase above Jungfraujoch. *Journal of Quantitative Spectroscopy*
606 *and Radiative Transfer*, 160:36–49.
- 607 Franco, B., Mahieu, E., Emmons, L. K., Tzompa-Sosa, Z. A., Fischer, E. V., Sudo, K.,
608 Bovy, B., Conway, S., Griffin, D., Hannigan, J. W., Strong, K., and Walker, K. A.
609 (2016). Evaluating ethane and methane emissions associated with the development
610 of oil and natural gas extraction in North America. *Environmental Research Letters*,

- 611 11(4):44010.
- 612 Friedrich, M., Beutner, E., Reuvers, H., Smeekes, S., Urbain, J.-P., Bader, W., Franco,
613 B., Lejeune, B., and Mahieu, E. (2020a). A statistical analysis of time trends in
614 atmospheric ethane. *Climatic Change*, 162:105–125.
- 615 Friedrich, M. and Lin, Y. (2024). Sieve bootstrap inference for linear time-varying
616 coefficient models. *Journal of Econometrics*, 239(1):105345.
- 617 Friedrich, M., Lin, Y., Ramdaras, P., Telg, S., and van der Sluis, B. (2025). Modelling
618 time-varying relations in housing prices: a semiparametric panel approach. *Journal*
619 *of the Royal Statistical Society Series C: Applied Statistics*, page qlaf020.
- 620 Friedrich, M., Smeekes, S., and Urbain, J. (2020b). Autoregressive wild bootstrap
621 inference for nonparametric trends. *Journal of Econometrics*, 214:81–109.
- 622 García, O. E., Schneider, M., Sepúlveda, E., Hase, F., Blumenstock, T., Cuevas, E.,
623 Ramos, R., Gross, J., Barthlott, S., Röhlting, A. N., Sanromá, E., González, Y.,
624 Gómez-Peláez, A. J., Navarro-Comas, M., Puenteadura, O., Yela, M., Redondas,
625 A., Carreño, V., León-Luis, S. F., Reyes, E., García, R. D., Rivas, P. P., Romero-
626 Campos, P. M., Torres, C., Prats, N., Hernández, M., and López, C. (2021). Twenty
627 years of ground-based NDACC FTIR spectrometry at Izaña observatory – overview
628 and long-term comparison to other techniques. *Atmospheric Chemistry and Physics*,
629 21(20):15519–15554.
- 630 Griffith, D. W. T., Deutscher, N. M., Velazco, V., Jones, N. B., Paton Walsh, C., and
631 Wilson, S. R. (2021). TCCON and NDACC: 20 years of ground-based remote sens-
632 ing of atmospheric trace gases at Wollongong and Darwin. *Baseline Atmospheric*
633 *Program Australia 2011-2013*, csiro:EP2021-3762:55.
- 634 Hannigan, J. W., Coffey, M. T., and Goldman, A. (2009). Semiautonomous FTS obser-
635 vation system for remote sensing of stratospheric and tropospheric gases. *Journal*
636 *of Atmospheric and Oceanic Technology*, 26(9):1814 – 1828.
- 637 Harvey, A., Koopman, S., and Riani, M. (1997). The modelling and seasonal
638 adjustment of weekly observations. *Journal of Business and Economic Statistics*,
639 15:354–368.
- 640 Harvey, A. C. (1989). *Forecasting, Structural Time Series Models and the Kalman*
641 *Filter*. Cambridge University Press, 1st edition.
- 642 Harvey, D. I. and Leybourne, S. J. (2014). Break date estimation for models with
643 deterministic structural change. *Oxford Bulletin of Economics and Statistics*,
644 76:623–642.
- 645 Hausmann, P., Sussmann, R., and Smale, D. (2016). Contribution of oil and natural
646 gas production to renewed increase in atmospheric methane (2007-2014): top-down
647 estimate from ethane and methane column observations. *Atmospheric Chemistry*
648 *and Physics*, 16(5):3227–3244.
- 649 Kiel, M., Hase, F., Blumenstock, T., and Kirner, O. (2016). Comparison of XCO
650 abundances from the total carbon column observing network and the network for the
651 detection of atmospheric composition change measured in Karlsruhe. *Atmospheric*
652 *Measurement Techniques*, 9(5):2223–2239.
- 653 Kivi, R. and Heikkinen, P. (2016). Fourier transform spectrometer measurements of
654 column CO₂ at Sodankylä, Finland. *Geoscientific Instrumentation, Methods and*
655 *Data Systems*, 5(2):271–279.

- 656 Li, D., Chen, J., and Gao, J. (2011). Non-parametric time-varying coefficient panel
657 data models with fixed effects. *Econometrics Journal*, 14(3):387–408.
- 658 Lin, Y., Song, M., and van der Sluis, B. (2025). Bootstrap inference for lin-
659 ear time-varying coefficient models in locally stationary time series. *Journal of*
660 *Computational and Graphical Statistics*, 34(2):654–667.
- 661 Lin, Y., van der Sluis, B., and Friedrich, M. (2023). Bootstrapping trending time-
662 varying coefficient panel models with missing observations. Tinbergen Institute
663 Discussion Paper, 2023-079/III.
- 664 Lutsch, E., Strong, K., Jones, D., Blumenstock, T., Conway, S., Fisher, J., Hanni-
665 gan, J., Hase, F., Kasai, Y., Mahieu, E., Makarova, M., Morino, I., Nagahama, T.,
666 Notholt, J., Ortega, I., Palm, M., Poberovskii, A., Sussmann, R., and Warneke, T.
667 (2020). Detection and attribution of wildfire pollution in the Arctic and north-
668 ern midlatitudes using a network of Fourier-transform infrared spectrometers and
669 GEOS-Chem. *Atmospheric Chemistry and Physics*, 20(20):12813–2851.
- 670 Maddanu, F. and Proietti, T. (2023). Trends in atmospheric ethane. *Climatic Change*,
671 176(5):1–23.
- 672 Makarova, M., Poberovskii, A., Polyakov, A., Imkhasin, K. H., Ionov, D., Makarov,
673 B., Kostsov, V., Foka, S., and Abakumov, E. (2024). Trends of key greenhouse gases
674 as measured in 2009-2022 at the FTIR station of St. Petersburg State University.
675 *Remote Sensing*, 16(11).
- 676 Ortega, I., Buchholz, R. R., Hall, E. G., Hurst, D. F., Jordan, A. F., and Hannigan,
677 J. W. (2019). Tropospheric water vapor profiles obtained with FTIR: comparison
678 with balloon-borne frost point hygrometers and influence on trace gas retrievals.
679 *Atmospheric Measurement Techniques*, 12(2):873–890.
- 680 Pardo Cantos, I., Mahieu, E., Chipperfield, M. P., Smale, D., Hannigan, J. W.,
681 Friedrich, M., Fraser, P., Krummel, P., Prignon, M., Makkor, J., Servais, C., and
682 Robinson, J. (2022). Determination and analysis of time series of CFC-11 (CCl₃F)
683 from FTIR solar spectra, in situ observations, and model data in the past 20
684 years above Jungfrauoch (46°N), Lauder (45°S), and Cape Grim (40°S) stations.
685 *Environmental Science: Atmospheres*, 2:1487–1501.
- 686 Perron, P. and Zhu, X. (2005). Structural breaks with deterministic and stochastic
687 trends. *Journal of Econometrics*, 129(1):65–119. Modelling structural breaks.
- 688 Proietti, T. (2000). Comparing seasonal components for structural time series models.
689 *International Journal of Forecasting*, 16:247–260.
- 690 Robinson, P. M. (1989). *Nonparametric estimation of time varying parameters*
691 *In: Hackl, P. (Ed.), Statistics, Analysis and Forecasting of Economic Structural*
692 *Change*. Springer, Berlin.
- 693 Szopa, S., Naik, V., Adhikary, B., Artaxo, P., Berntsen, T., Collins, W., Fuzzi, S.,
694 Gallardo, L., Kiendler-Scharr, A., Klimont, Z., Liao, H., Unger, N., and Zanis, P.
695 (2021). Short-lived climate forcers. climate change 2021: The physical science basis.
696 Contribution of Working Group I to the Sixth assessment report of the intergovern-
697 mental panel on climate change. *Cambridge University Press, Cambridge, United*
698 *Kingdom and New York, NY, USA*, pages 817–922.
- 699 Vigouroux, C., Stavrakou, T., Whaley, C., Dils, B., Duflot, V., Hermans, C., Kumps,
700 N., Metzger, J.-M., Scolas, F., Vanhaelewyn, G., Müller, J.-F., Jones, D. B. A.,

- 701 Li, Q., and De Mazière, M. (2012). FTIR time-series of biomass burning products
702 (HCN, C₂H₆, C₂H₂, CH₃OH, and HCOOH) at Reunion Island (21° S, 55° E) and
703 comparisons with model data. *Atmospheric Chemistry and Physics*, 12(21):10367–
704 10385.
- 705 Xiao, Y., Logan, J., Jacob, D., Hudman, R., Yantosca, R., and Blake, D. (2008). Global
706 budget of ethane and regional constraints on U.S. sources. *Journal of Geophysical
707 Research*, 113:D21306.
- 708 Yamanouchi, S., Conway, S., Strong, K., Colebatch, O., Lutsch, E., Roche, S., Taylor,
709 J., Whaley, C. H., and Wiacek, A. (2023). Network for the detection of atmospheric
710 composition change (NDACC) fourier transform infrared (FTIR) trace gas mea-
711 surements at the University of Toronto atmospheric observatory from 2002 to 2020.
712 *Earth System Science Data*, 15(8):3387–3418.
- 713 Yurganov, L. N., Blumenstock, T., Grechko, E. I., Hase, F., Hyer, E. J., Kasischke,
714 I. S., Koike, M., Kondo, Y., Kramer, I., Leung, F.-Y., Mahieu, E., Mellqvist, J.,
715 Notholt, J., Novelli, P. C., Rinsland, C. P., Scheel, H. E., Schulz, A., Strand-
716 berg, A., Sussmann, R., Tanimoto, H., Velazco, V., Zander, R., and Zhao, Y.
717 (2004). A quantitative assessment of the 1998 carbon monoxide emission anomaly
718 in the Northern Hemisphere based on total column and surface concentration
719 measurements. *Journal of Geophysical Research*, 109:D15305.
- 720 Yurganov, L. N., Duchatelet, P., Dzhola, A. V., Edwards, D. P., Hase, F., Kramer, I.,
721 Mahieu, E., Mellqvist, J., Notholt, J., Novelli, P. C., Rockmann, A., Scheel, H. E.,
722 Schneider, M., Schulz, A., Strandberg, A., Sussmann, R., Tanimoto, H., Velazco,
723 V., Drummond, J. R., and Gille, J. C. (2005). Increased Northern Hemispheric
724 carbon monoxide burden in the troposphere in 2002 and 2003 detected from the
725 ground and from space. *Atmospheric Chemistry and Physics*, 5(2):563–573.
- 726 Zander, R., Mahieu, E., Demoulin, P., Duchatelet, P., Roland, G., Servais, C.,
727 De Mazière, M., Reimann, S., and Rinsland, C. (2008). Our changing atmosphere:
728 Evidence based on long-term infrared solar observations at the Jungfrauoch since
729 1950. *Science of The Total Environment*, 391(2-3):184–195.
- 730 Zeng, G., Wood, S. W., Morgenstern, O., Jones, N. B., Robinson, J., and Smale, D.
731 (2012). Trends and variations in CO, C₂H₆, and HCN in the Southern Hemisphere
732 point to the declining anthropogenic emissions of CO and C₂H₆. *Atmospheric
733 Chemistry and Physics*, 12(16):7543–7555.
- 734 Zhang, M., Vimont, I. J., Jordaan, S. M., Hu, L., McKain, K., Croftwell, M.,
735 Gaeta, D. C., and Miller, S. M. (2024). U.s. ethane emissions and trends esti-
736 mated from atmospheric observations. *Environmental Science & Technology*,
737 58(35):15539–15550. PMID: 39169712.
- 738 Zhou, M., Langerock, B., Wang, P., Vigouroux, C., Ni, Q., Hermans, C., Dils, B.,
739 Kumps, N., Nan, W., and De Mazière, M. (2023). Understanding the variations
740 and sources of CO, C₂H₂, C₂H₆, H₂CO, and HCN columns based on 3 years of
741 new ground-based Fourier transform infrared measurements at Xianghe, China.
742 *Atmospheric Measurement Techniques*, 16(2):273–293.